Transition between quasi 2D and 3D Rayleigh-Bénard convection in a horizontal magnetic field

Vogt, T.; Ishimi, W.; Yanagisawa, T.; Tasaka, Y.; Sakuraba, A.; Eckert, S.;

Originally published:

January 2018

Physical Review Fluids 3(2018), 013503

DOI: https://doi.org/10.1103/PhysRevFluids.3.013503

Transition between quasi 2D and 3D Rayleigh-Bénard convection in a horizontal magnetic field

Tobias Vogt[1], Wataru Ishimi[2], Takatoshi Yanagisawa[3], Yuji Tasaka[2], Ataru Sakuraba[4], Sven Eckert[1]
[1]Helmholtz Zentrum Dresden-Rossendorf (HZDR), Dresden, Germany
[2]Laboratory for Flow Control, Hokkaido University, Sapporo, Japan
[3]Japan Agency for Marine-Earth Science and Technology (JAMSTEC), Yokosuka, Japan
[4] Department of Earth and Planetary Science, University of Tokyo, Tokyo, Japan

Abstract

MHD Rayleigh-Bénard convection was studied experimentally and numerically using a liquid metal inside a box with square horizontal cross section and aspect ratio five. Applying a sufficiently strong horizontal magnetic field converts the convective motion into a flow pattern of quasi-two dimensional rolls arranged parallel to the magnetic field. The aim of this paper is to provide a detailed description of the flow field, which is often considered as quasi 2D. In this paper we focus on the transition from a quasi-two-dimensional state towards a three-dimensional flow occurring with decreasing magnetic field strength. We present systematic flow measurements that were performed by means of ultrasound Doppler velocimetry. The measured data give an insight into the dynamics of the primary convection rolls, the secondary flow induced by Ekman pumping and reveal the existence of small vortices that develop around the convection rolls. The flow measurements are completed by direct numerical simulations. Numerical results and experimental findings show an excellent agreement with respect to the qualitative flow features.

1. Introduction

One of the classical problems in fluid dynamics is the Rayleigh-Bénard convection (RBC) where a fluid layer is exposed to a temperature difference ΔT between a colder lid and a warmer bottom. Various RBC regimes are defined by the Rayleigh number, $\mathrm{Ra} = \alpha g \Delta T H^3/\kappa\nu$, the Prandtl number, $\mathrm{Pr} = \nu/\kappa$, and the geometry of the fluid vessel. In these formulae, α, κ, ν are the volumetric coefficient of thermal expansion, thermal diffusivity, and kinematic viscosity of the fluid, respectively, and g and H are the gravity acceleration and height of the fluid layer, respectively. Numerous studies about RBC have been published so far, an introduction and overview can be found in [1,2]. Effects arising from external forces such as magnetic fields [3,4] or vessel rotation [5,6] attracted growing interest among the scientific community. For instance, an extension of the Lohse-Grossmann theory to the magnetohydrodynamic (MHD) case has been suggested recently [7]. The present experimental and numerical study considers the specific case of liquid metal convection under the influence of a DC magnetic field [8]. The effect of the magnetic field is quantified by the dimensionless Chandrasekhar number $Q = B^2H^2\sigma/\rho\nu$ which is the Hartmann number Ha squared. It represents the ratio of the electromagnetic force to the viscous force, where σ and ρ are the electric conductivity and density of the fluid, respectively, and B is the strength of the

applied magnetic field. The magnetic field in our experiments is applied in horizontal direction perpendicular to the temperature gradient. A sufficiently strong magnetic field causes a two-dimensional convection pattern in a way that the convection rolls are oriented along the magnetic field lines. The corresponding flow regime diagram of the convection patterns was reported in a recent paper [9]. This regime diagram reveals a multitude of flow structures governed by the balance between Lorenz force and the buoyancy and it illustrates the selection criterion for the roll number depending on *Ra* and *Q*. Further previous studies presented essential features of various regimes and regime transitions including the characteristic phenomena of "flow reversals" occurring at specific selections of *Ra* and *Q* [10-12]. These flow reversals are distinguished by spontaneous changes of the rotational direction of the convection rolls and might be caused by the oscillatory instability and the skewed-varicose instability both of which affect the quasi two-dimensional rolls.

In general, the application of the DC magnetic field generates a Lorentz force which strongly attenuates angular momentum perpendicular to the field lines by Joule dissipation [13]. The Joule dissipation would vanish for a perfectly 2D configuration of an infinite roll length, where the electrical potential cannot drive current loops. Owing to this mechanism, the flow field tends to become uniform along the magnetic field direction. However, the anisotropy of the flow field does not necessarily mean that the velocity component parallel to the field vanishes. Since we consider the convection in a box with a square cross section, the convection rolls are confined by no slip boundaries. The differential rotation of the fluid particles at those solid walls at the end of the convection rolls produces a converging flow in the boundary layer, called Ekman pumping [14]. The thickness of the so-called Ekman layer follows from the relation $\delta_E \sim (\nu/\Omega)^{1/2}$ where Ω stands for the rotation rate of the convection rolls. Due to continuity, the Ekman pumping is responsible for driving a secondary loop inside the fluid vessel. In the flow configuration considered here, the Ekman pumping happens at the sidewalls perpendicular to the magnetic field lines. Hence, the near sidewall region is also covered by the Hartmann layers where the electromagnetic force and viscous friction balance each other out. Because the side walls perpendicular to the magnetic field are electrically non-conducting in our experiment the induced electric currents close exclusively within the Hartmann layers [3]. These Hartmann layers are in the order of $O(Ha^{-1})$ [15] and become quite thin for high Hartmann numbers. Their influence on the flow has to be considered in relation to the boundary layers created by Ekman pumping. A detailed theoretical analysis of Ekman pumping in Hartmann layers can be found in [16]. Furthermore, a recent study considered the role of Ekman pumping in the context of the dimensionality of a single electrically driven vortex bounded by two horizontal walls [17].

For a decreasing intensity of the magnetic field at a given *Ra* number, an initially stable quasi-2D structure of convection rolls arranged parallel to the magnetic field will become unstable and tend to develop 3D perturbations. The secondary flow generated by Ekman pumping is supposed to play an essential role during the transition from a quasi-two-dimensional towards a three-dimensional flow field.

There is still a rather limited knowledge concerning the development of 3D flow structures in RBC under the impact of a horizontal DC magnetic field. In this paper, we provide a detailed

representation of 3D flow structures by measuring the spatiotemporal flow velocity maps parallel and perpendicular to the magnetic field lines. The flow velocities are acquired by means of the Ultrasound-Doppler-Velocimetry (UDV), which is an attractive tool for visualizing flow patterns in opaque fluids like liquid metals. The experimental work is complemented by direct-numerical simulations which enable a better intuitive understanding of the complex flow structures.

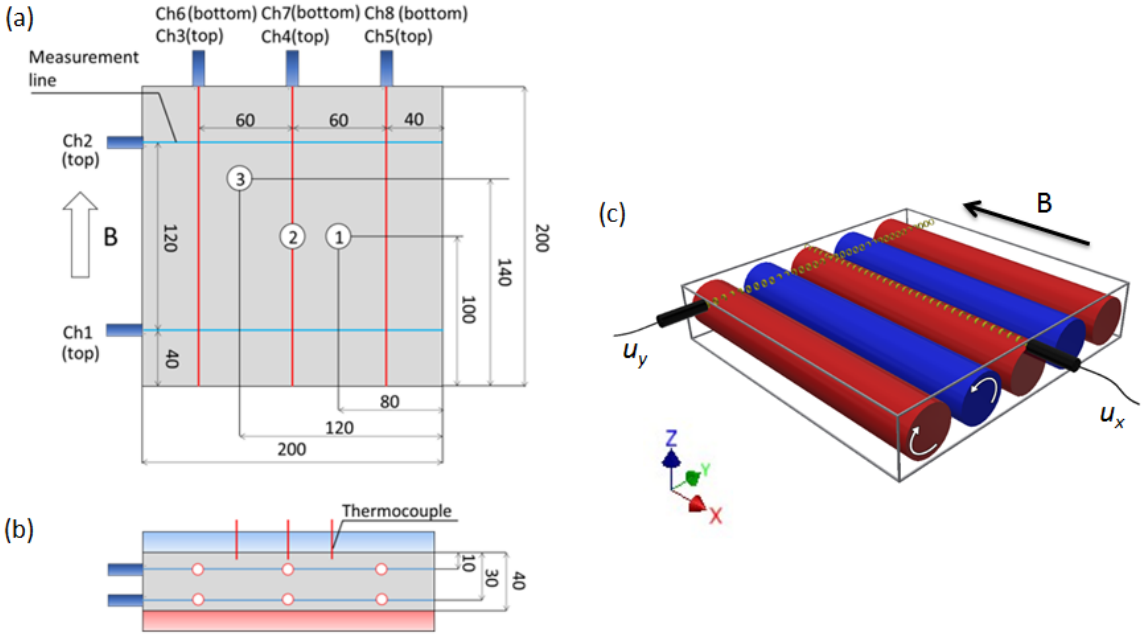

Figure 1. Experimental setup in top view (a) and side view (b). The dimensions are in mm. Schematic drawing of the counter rotating convection rolls and UDV measuring lines (c)

2. Experimental setup and numerical simulation

2.1 Experimental setup and procedure

The temperature and flow measurements reported within this paper were conducted by means of the same experimental setup as used in a previous work [12]. The eutectic alloy GaInSn, that has a melting temperature of T_0 = 10.5 °C, is filled in a rectangular vessel that has an inner cross section of 200 mm × 200 mm and a height of 40 mm, giving an aspect-ratio of five (see Fig. 1). At room temperature, the metal alloy has approximately one-third the viscosity of water ($\nu = 3.4 \times 10^{-7}$ m²/s), a density of $\rho = 6360$ kg/m³ and an electrical conductivity of $\sigma = 3.2 \times 10^{6}$ S/m. The thermal diffusivity is $\kappa = 1.05 \times 10^{-5}$ m²/s and the thermal expansion coefficient is $\alpha = 1.24 \times 10^{-4}$ 1/K [18]. Accordingly, the *Pr* is about 0.03. The sidewalls of the insulating vessel are made of polyvinyl chloride (PVC), whereas the top and bottom plate are made of copper. The temperature of both copper plates can be controlled by water that is pumped through channels inside the plates. The copper plates have about 20 times the thermal conductivity of GaInSn. The filled vessel is located inside a DC inductor that creates a

horizontal magnetic field up to 350 mT. Measurements of the field strength showed non-uniformities up to 5 % throughout the measuring volume.

Two of the vessel sidewalls are equipped with ultrasound transducers (Ch1-Ch8, see Fig. 1) in order to measure the fluid velocities parallel and perpendicular to the magnetic field lines. The transducers are connected to a DOP 2000 velocimeter (model 2125, Signal Processing SA, Lausanne). The spatial resolution of the velocity measurements is about 1 mm in axial direction and 5 mm in lateral direction, whereas a temporal resolution of about 1 Hz has been realized. The transducers are in direct contact with the fluid in order to ensure a good acoustic transmission for enabling the acquisition of velocity data with satisfying quality even at low liquid velocities of about 0.5 mm/s. The applied sensor positions are shown in Fig. 1(a), (b). We used custom-built transducers (Fa. Richter) made without any ferromagnetic parts in order to achieve a good measuring quality in the presence of strong magnetic fields.

The temperatures of the bottom and top plates where measured with one thermocouple each embedded in the copper plates. The temperatures inside the fluid were measured at three different positions (see Fig. 1) in a 3 mm distance from the upper boundary by means of thermocouples as well. The temporal resolution of the temperature measurements is about 10 Hz.

2.2 Method of numerical simulation

We performed direct numerical simulations for the same geometry as in the laboratory experiment, considering a horizontal magnetic field imposed on the rectangular vessel of no-slip velocity boundaries. The main motivation for the numerical simulation was to improve the understanding of the complex 3D effects, especially by revealing the complete flow structure in the entire vessel. The code used here is identical to [11], and reproduced successfully the Ra and Q dependence for the convection regimes. In the code, a set of magnetohydrodynamic equations is solved by a finite difference method using a uniform grid interval. The adopted vertical grid points are 48, 64 and 120, depending on the value of Ra and Q. As the aspect ratio of the vessel is five, the horizontal grid points are 240, 320, and 600, respectively. The value of Pr for the simulation is 0.025. In these simulations, the length and time are nondimensionalized by the layer thickness H and the thermal diffusion time $\tau_\kappa = H^2/\kappa$, respectively. The time unit corresponds to $\tau_\kappa = 152$ s and the velocity unit to $U = H/\tau_\kappa = 0.26$ mm/s. For more details and information with respect to a verification of the code the reader is referred to [11].

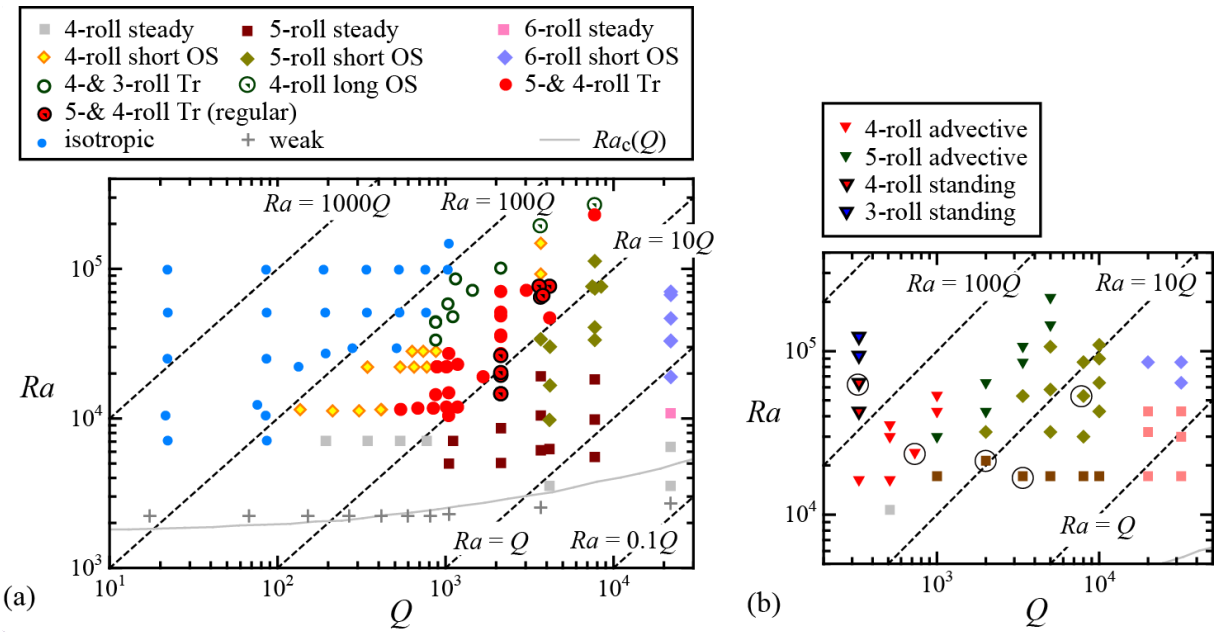

Figure 2: (a) Regime diagram of the liquid metal RBC exposed to a horizontal magnetic field replotted from [12], where the grey line represents the expected neutral stability curve for the vessel with aspect ratio five based on the result in [3]. (b) parameter points of flow measurements carried out within this study, whereas the circled symbols mark the measurements to be presented in the next paragraph.

3. Results

Figure 2(a) shows the regime diagram replotted from [12]. As distinct from the preceding paper here we use material property data for GaInSn taken from a more recent publication [18]. Depending on the choice of Ra and Q diverse flow regimes can be observed ranging from isotropic pattern without a preferred orientation of the convection rolls through to 6-roll structures strictly aligned parallel to the magnetic field. Previous studies indicate that the transitions between the main regimes obviously occur along lines of Ra/Q = constant [9, 11, 12]. Above Ra/Q = 100, the magnetic field appears to be too weak to provoke any significant changes of the isotropic flow pattern. Here, the convection rolls do not show a preferred orientation. Below Ra/Q =100, the convection rolls become aligned parallel to the magnetic field lines. The first stable flow configuration that can be observed in our system at Ra/Q < 100 is a 4-roll configuration. If the magnetic field is further increased (Ra/Q < 10), the most stable flow configuration was found at 5-rolls. As soon as the magnetic field aligns the convection rolls with the magnetic field lines, the flow components perpendicular to the magnetic field become dominant whereas the flow parallel to B becomes weak. The later, however, is not negligible. In order to reconstruct a complete figure of the considered flow, both velocity components parallel and perpendicular to the magnetic field have been measured. Prominent features of the flow structure will be discussed below.

Figure 2(b) contains a section of the regime diagram showing the parameter range covered by this study. In this paper, we selected exemplary cases for studying the gradual loss of stability

of the quasi 2D roll pattern with decreasing impact of the magnetic field. For that purpose, we increased stepwise the ratio *Ra/Q* and focused especially on measurements of the axial velocity u_x parallel to convection rolls in order to reliably detect early deviations from the 2D state. The particular measurements to be presented in the next section are highlighted by encircled symbols. On the route from quasi-2D structures to 3D ones we identified four different regimes for the first time on the basis of flow measurements along the direction of the magnetic field. Referring to data obtained by the measurements perpendicular to the field, the flow structure can be classified being a 4-roll short OS regime according to figure 2(a) and already known from former studies. The analysis of the axial flow component discloses that this regime can be subdivided into two further regimes. While the oscillations of the primary flow structure remain two-dimensional for $Ra/Q < 10$, two new regimes have been identified for $Ra/Q \geq 40$, named as 4-roll advective and 4-roll standing wave regime, respectively. Here, the flow measurements demonstrate clear deviations from two-dimensionality. Although not shown as flow measurement in this paper a 3-roll standing wave regime is also newly observed for $Ra/Q > 300$.

3.1 Velocity measurements

Figure 3(a) shows a measurement of the u_y - component (perpendicular to *B*) of a very stable 5-roll configuration, which is an example of "5-roll steady" regime. This data set was recorded along the measuring line of Ch2 (see Fig. 1(a)) at $Ra = 1.7 \times 10^4$ and $Q = 3.4 \times 10^3$ which corresponds to $Ra/Q = 5.1$. A negative velocity (blue) indicates a flow towards the sensor while positive velocities (red) stand for movements away from the sensor. The maximal velocity in Fig. 3(a) is about ± 4.7 mm/s, whereby the measuring line is 10 mm shifted with respect to the roll center. The angular speed of the roll can be estimated according to $\omega \approx 4.7 \text{ mm/s} \times (2\pi \times 10 \text{ mm})^{-1} = 0.075$ Hz; leading to a circulation period of 13 s for one rotation.

Figure 3 (b) shows the velocity components parallel to the magnetic field lines (u_x) measured by Ch7 (see Fig. 1(a)). It reveals a two-cell structure being symmetric with respect to the middle of the fluid vessel. The velocities parallel to *B* reach values around 1/6th of the velocities perpendicular to *B*. A similar symmetric distribution of the velocity components parallel to the magnetic field lines is obtained at the other UDV channel Ch8, as shown in Figure 3 (c). The magnitude of the velocity is almost the same as for Ch7, but the flow direction is completely opposite. The transducer positions Ch7 and Ch8 are marked in Fig. 3(a) by dashed lines. In a five-roll arrangement the position of transducer Ch7 coincides with the middle of the third convection roll, whereas the measuring line for Ch8 proceeds almost exactly between two neighbouring convection rolls. The Figs. 3(b) and 3(c) demonstrate that inside the convection rolls the secondary flow parallel to the magnetic field is directed from the Ekman layers towards the center of the fluid vessel and it comes back to the wall along the rim of rolls.

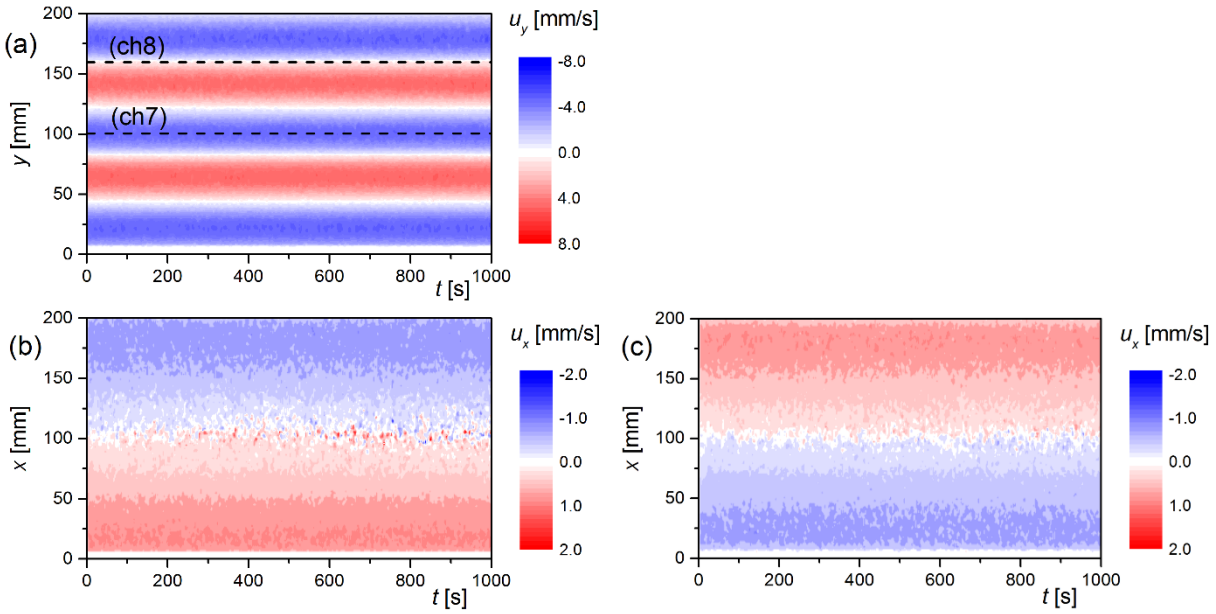

Figure 3: Flow measurement at Q = 3.4 × 10^3 and Ra = 1.7 × 10^4 (5-roll steady). (a) (Ch2): Fluid velocity perpendicular to the magnetic field, (b) (Ch7) and (c) (Ch8): Fluid velocity measured along the magnetic field lines. Ra/Q = 5.1

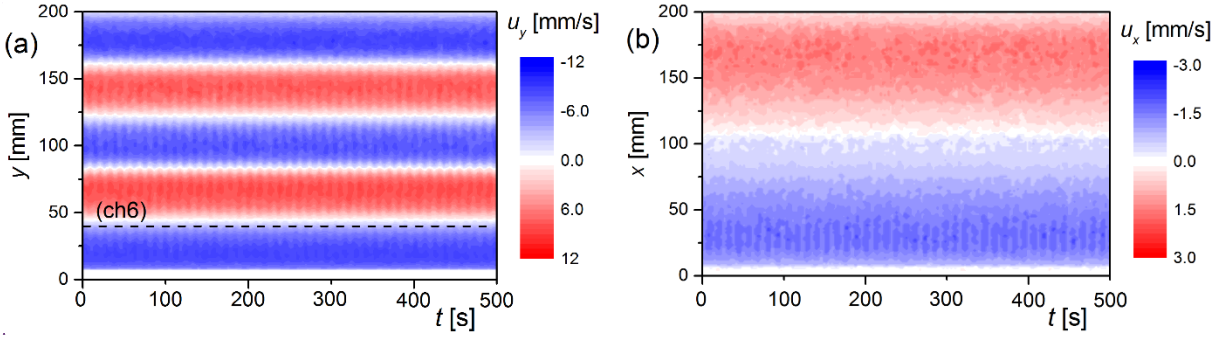

Figure 4: Flow measurement at Q = 8.0 × 10^3 and Ra = 5.5 × 10^4 (5-roll short OS). (a) (Ch2) Fluid velocity perpendicular to the magnetic field, (b) (Ch6) Fluid velocity measured along the magnetic field lines. Ra/Q = 6.9

Figure 4 shows a measurement obtained at a slightly higher Ra/Q ratio, at Rayleigh number (Ra = 5.5 × 10^4) and Chandrasekhar number (Q = 8.0 × 10^3). The higher temperature difference imposed here results in higher fluid velocities compared to the experiment presented in Fig. 3. On the other hand, the increased magnetic field strength stabilizes the convection rolls. A detailed consideration of Fig. 4(a) reveals a slight but regular oscillation which appears in both flow directions (u_y and u_x). This case belongs to "5-roll short OS" regime. This oscillation can be associated with a deformation of the rolls from a circular towards an elliptical cross section [12].

Figure 4(b) shows the flow field parallel to the magnetic field measured by transducer Ch6. The ratio of the velocities u_x/u_y is about 1/5 and the influence of short-period oscillation can also be seen here. The basic structure of the flow field in the direction of B remains the same as shown in Fig. 3(b) and (c).

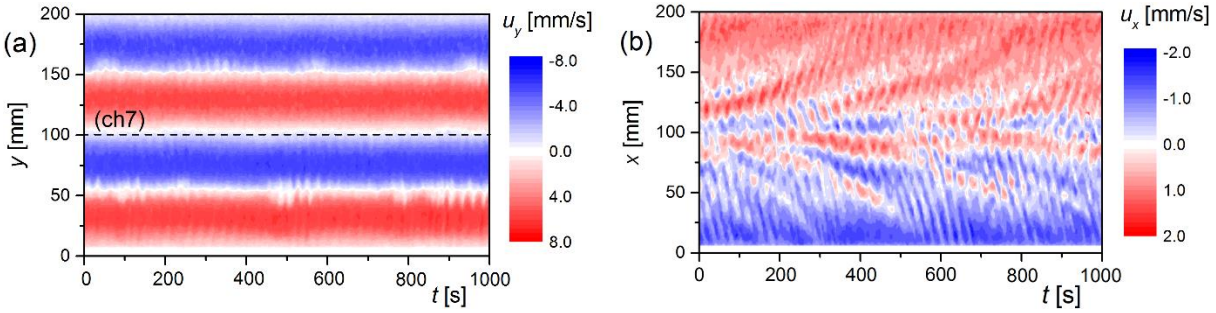

Figure 5: Flow measurement at $Q = 7.3 \times 10^2$ and $Ra = 2.4 \times 10^4$ (4-roll advective). (a) (Ch2) Fluid velocity perpendicular to the magnetic field, (b) (Ch7) Fluid velocity measured along the magnetic field lines. $Ra/Q = 33$

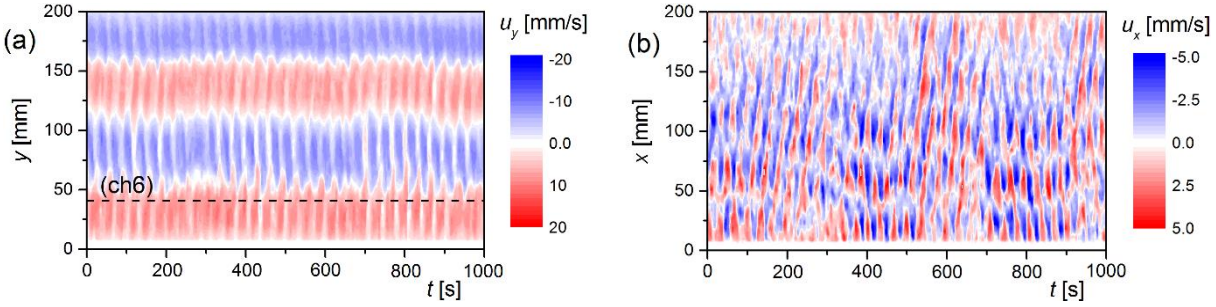

Figure 6: Flow measurement at $Q = 3.3 \times 10^2$ and $Ra = 6.7 \times 10^4$ (4-roll standing). (a) (Ch2) Fluid velocity perpendicular to the magnetic field, right: (Ch6) Fluid velocity measured along the magnetic field lines. $Ra/Q = 203$

The measurement shown in Fig. 5 was recorded at a much higher Ra/Q - ratio of 33 ($Q = 7.3 \times 10^2$ and $Ra = 2.4 \times 10^4$). Hence, the stabilizing effect of the magnetic field becomes weaker. The increase of Ra/Q is associated with a change of the convection pattern to a 4-roll configuration. The most significant change, however, can be detected in the u_x- velocity field (see Fig 5(b)). The flow field in the direction of B is now superimposed by some vortex substructures that emerge in the center of the cell. After their formation, the vortices are captured by the diverging axial flow and are transported in direction to either of the sidewalls of the cell. This is a significant feature of newly identified "4-roll advective" regime. Obviously, the sideward movement of the emerging vortices occurs in alternating directions and the advection speed of the vortices increases the closer they come to the sidewalls, as indicated by the curved path of the vortices. The visual manifestation of the vortices in this spatio-temporal velocity plot and their behaviour in the axial recirculation shows distinct

similarities to Taylor-Görtler vortices in a transitional rotating liquid metal flow that was driven by a rotating magnetic field [19].

In contrast to the u_x-velocity field, the vortices are not visible in the u_y-velocity field (see Fig. 5(a)). The configuration of the four convection rolls looks rather stable. Only some weak disturbances appear between neighbouring rolls. Short-term oscillations of the flow become visible just as in the case of the five-roll regime at lower *Ra/Q* in Fig. 4. These oscillations appear to be much more pronounced in the axial flow shown in Fig. 5(b). The ratio of the velocities u_x/u_y is about 1/5 again.

A further increase of *Ra/Q* to a value of 203 leads to the flow pattern displayed in Fig. 6 ($Q = 3.3 \times 10^2$ and $Ra = 6.7 \times 10^4$). In the regime diagram shown in Fig. 2(a), this *Ra/Q* – ratio is indicated to be situated in the "isotropic" domain of thermal turbulence where the flow is expected to lose its orientation with respect to the direction of *B*. However, the flow in Fig. 6 cannot be classified as fully isotropic since the roll structure still exists in this state (see Fig. 6(a)). It was observed that 4-roll structure is kept for this region with stepwise increase of *Ra*/*Q*. Strong oscillations become apparent showing significantly larger periods than the oscillating pattern in Fig. 4. Besides these almost regular fluctuations a long-period modulation with respect to the roll size and position can be noticed. Overlooking Fig. 6(b) makes clear that the structure of the axial flow component is dominated by the same type of oscillations. We suggest ascribing these flow features to the occurrence of standing waves in this parameter region. We classified this case as a "4-roll standing" regime. The ratio of $u_x/u_y = 1/2$ in Fig. 6 is considerably higher as in the examples shown before. The spatio-temporal structure of the axial flow parallel to the magnetic field can be divided into four or five subdomains where the flow direction changes periodically. Apparently, this behaviour is synchronized with slight modulations in the main roll structure. We observed similar standing waves accompanied with a 3-roll structure at higher *Ra*/*Q* as indicated in Fig. 2(b). All in all, these observations provide strong indications for a flow transition from a quasi-two dimensional to a three-dimensional state.

3.2 Temperature measurements

Figure 7 shows a set of temperature measurements conducted at constant Q (3.4×10^3) and varying Ra-numbers. The time series presented in Figs. 7(a) – (d) were taken from a long-term measurement where *Ra* was increased stepwise. Any transient period after increasing of *Ra* was not taken into account here in order to ensure equilibrium conditions. Time stamps of each figure are taken over from the original single record. Simultaneous measurements by UDV (not shown here) confirm that the flow maintained a stable 5-roll structure for all *Ra*-numbers applied throughout the experiment. In general, four different temperature regimes can be distinguished in this figure. If the *Ra*-number is below a certain threshold, the temperatures in the fluid are steady (Fig 7(a); 5-roll steady). If the *Ra*-number is increased, short period oscillations appear (Fig 7(b); 5-roll short OS). The short period oscillations are superimposed by long period oscillations if the *Ra*-number is further increased (Fig 7(c); 5-

roll advective). The short and long period oscillations are replaced by irregular temperature fluctuations at even higher Ra-numbers (Fig 7(d); also 5-roll advective). In this measurement, the shape of the temperature variations depends on the sensor positions too; irregular fluctuations with negative and positive spikes are found for the sensor 1 and 3, whereas intermittent regular fluctuations are observed for the sensor 2. The sensors 1 and 3 are located at the boundary region between two neighbouring convection rolls and the position of sensor 2 corresponds to the centre of the roll, respectively. In case of variable roll positions, as shown for instance in Fig. 5(a), the relative position of the sensors with respect to the roll location would change causing related temperature variations.

The development of temperature fluctuations observed within this study is rather similar to corresponding results reported in [3] for a wider container.

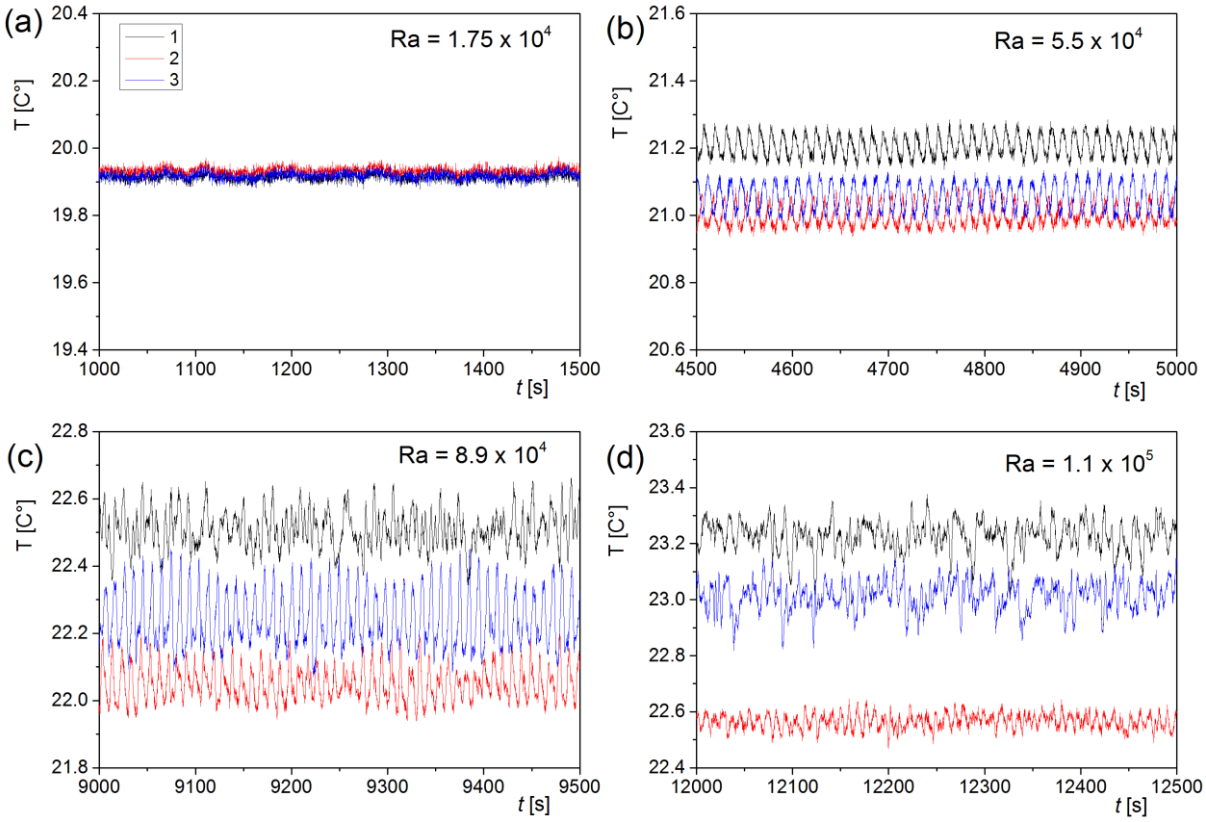

Figure 7: Temperature measurements showing the different temperature regimes for $Q = 3.4 \times 10^3$: (a) $Ra = 1.75 \times 10^4$, $Ra/Q = 5.14$, (b) $Ra = 5.5 \times 10^4$, $Ra/Q = 16.2$, (c) $Ra = 8.9 \times 10^4$, $Ra/Q = 26.2$, (d) $Ra = 1.1 \times 10^5$, $Ra/Q = 32.4$, the positions of the thermocouples 1-3 are shown in Fig. 1.

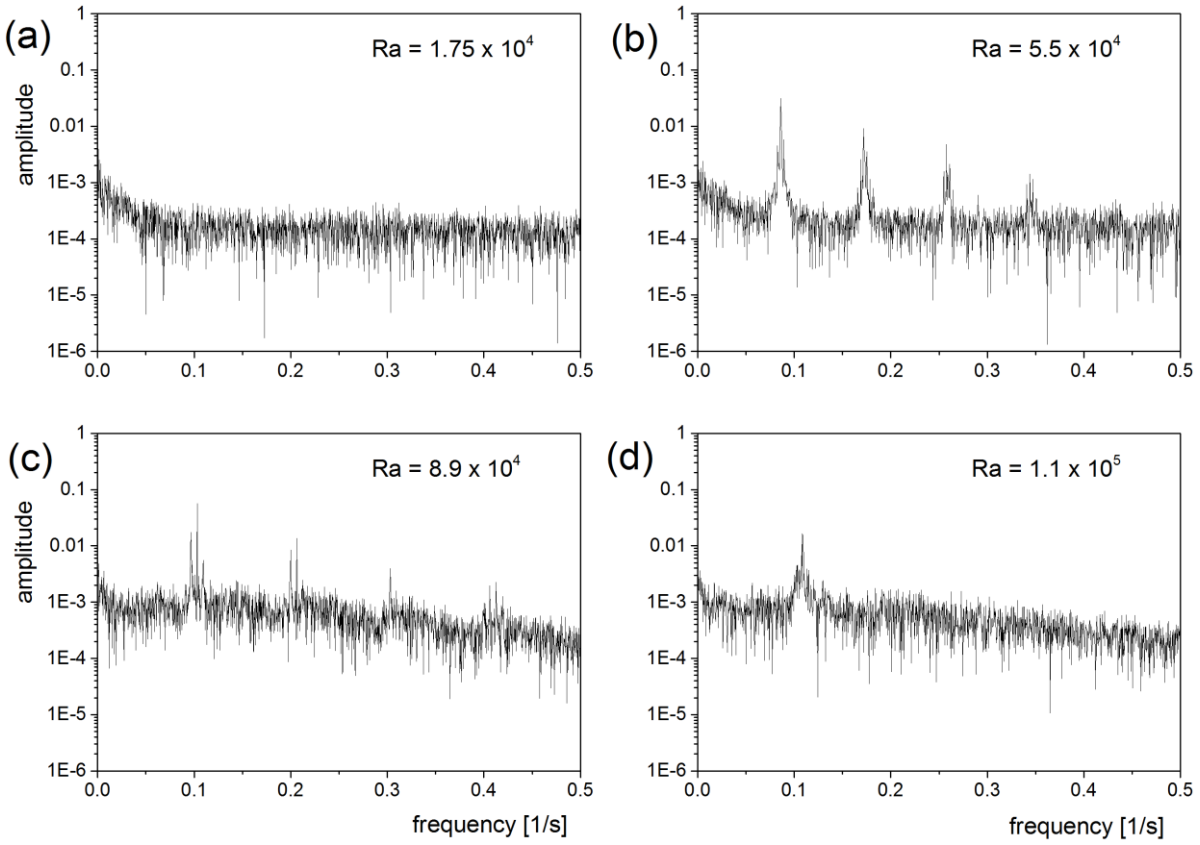

Figure 8: Temperature spectra corresponding to Fig. 7 for $Q = 3.4 \times 10^3$ (thermocouple 2): (a) $Ra = 1.75 \times 10^4$, $Ra/Q = 5.14$, (b) $Ra = 5.5 \times 10^4$, $Ra/Q = 16.2$, (c) $Ra = 8.9 \times 10^4$, $Ra/Q = 26.2$, (d) $Ra = 1.1 \times 10^5$, $Ra/Q = 32.4$.

Corresponding power spectra of the temperature signal for the different regimes are presented in Fig. 8. The regime at $Ra = 1.75 \times 10^4$ in Fig. 8(a), which has been associated with the existence of stationary rolls, does not exhibit clear peaks. The short period oscillation regime at $Ra = 5.5 \times 10^4$ in Fig. 8(b) contains a clear peak corresponding to the oscillation frequency of the rolls, $f_{os} = 0.086$ Hz, and its harmonics, e.g., $2f_{os}$. The main peak at f_{os} has sideband frequencies at $f_{os} - f_m = 0.083$ Hz and $f_{os} + f_m = 0.089$Hz ($f_m \sim 0.003$ Hz). These sidebands become clearer at $Ra = 8.9 \times 10^4$ as $f_{os} = 0.103$ and $f_{os} \pm f_m = 0.097$ and 0.110 Hz ($f_m \sim 0.006$ Hz), instead the contributions by higher harmonics are weakened. The sidebands in Fig. 8(b) and (c) are represented as amplitude modulations in Fig. 7, and indicate a low frequency modulation of the short period oscillations. This fact could be explained by an axial propagation of waves along the rolls with a frequency f_m. The modulation is hidden in the wide slope of the main frequency component, $f = 0.109$ Hz, at $Ra = 1.1 \times 10^5$.

4. Development of the flow structure during the transition from a quasi-two-dimensional towards a three-dimensional state

The experimental results presented in the last section, demonstrate the existence of different flow regimes characterized by different length and time scales. In this chapter, we want to gain a deeper insight into the features of the diverse flow structures illustrating the transition from a quasi-two-dimensional flow field to a three-dimensional one. At first, we want to discuss the role of the Ekman pumping. Then, the results of our numerical simulations will be presented rendering the details of the 3D velocity fields visible.

4.1 Steady rolls with superimposed axial flow: the relevance of Ekman pumping

The source of the axial flow component (u_x) can be found in the boundary layers where the convection rolls touch the vessel walls. The imbalance between the centrifugal forces and the radial pressure gradient in the boundary layer drives the fluid radially inwards and establishes, required by continuity, a secondary circulation. Irrespective of the rotational direction, the direction of the secondary circulation in the steady state is such that the flow within the boundary layers is converging towards the axis of the convection roll. From here the fluid is pumped towards the mid-plane of the fluid vessel and it streams back to the sidewalls along the rim of the convection rolls and within the space left between neighbouring rolls (see also Fig. 9). Two toroidal vortices are formed along each convection roll. These vortices are symmetric with respect to the horizontal mid-plane of the fluid vessel. The experimentally determined velocity date presented in the Figs. 3(b) and (c) are consistent with the schematic drawing in Fig. 9 which also explains the strong dependence of the flow pattern on the sensor position. Consequently, this secondary flow is an inherent feature of any rotating flow confined by and oriented perpendicular to two parallel end walls.

The horizontal circulating flow arising from the Ekman pumping is illustrated in Fig. (9), where u_e and δ indicate the characteristic velocity for Ekman pumping and the boundary layer thickness on the wall perpendicular to the magnetic field, respectively. In the case considered here, this boundary layer corresponds to the Hartmann layer.

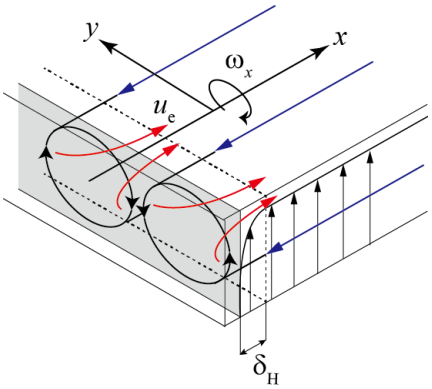

Figure 9: Illustration of the axial flow parallel to the magnetic field inside the convection rolls

The path length of this Ekman induced recirculation is about 2 × 100 mm for each circulation loop. From the measurements shown in Fig. 3(b) the average velocity of $\bar{u}_x = 0.4$ mm/s can be estimated resulting in a recirculation time of approximately 500 s.

In a next step, we want to focus on the ratio between the typical velocities for the Ekman pumping u_e and the RB convection rolls u_y. In general, the velocity of the Ekman pumping induced recirculation in rotating flows can be considered to be proportional to the boundary layer thickness δ and the vorticity ω_x:

$$u_e \sim \tfrac{1}{2}\delta\omega_x \qquad (1)$$

In the case considered here, two boundary layers occur at the side walls perpendicular to the magnetic field, the Ekman layer $\delta_E = \sqrt{\nu/\Omega}$ (with the angular velocity Ω) and the Hartmann layer $\delta_H = H/Q^{1/2}$. For sufficiently large Chandrasekhar numbers $Q >> Ra$ the thickness of the Hartmann layer is supposed to be considerably thinner as the Ekman layer. Then, the symbol δ in equation (1) can be replaced by the thickness of the Hartman boundary layer δ_H. With assuming $\omega_x \sim u_y/H$ the estimation becomes

$$u_e/u_y \sim Q^{-1/2}. \qquad (2)$$

Here, the influence of *Ra* becomes manifest on u_y only.

Figure 10(a) compares the estimated thickness of the Ekman layer δ_E and the Hartmann layer δ_H for different experiments carried out at various Chandrasekhar numbers with $Ra \sim 2 \times 10^4$. It becomes obvious that for $Q > 4 \times 10^3$ the value for δ_H falls below δ_E. The representative velocity for the Ekman pumping flow, u_e, calculated from the experimental, time-averaged velocity profiles $\bar{u}_x(x)$, the typical rotating velocity of the convection rolls, $\bar{u}_{y,max}$, and the ratio $u_e/\bar{u}_{y,max}$ are shown in Fig. 10(b). The analysis is restricted to data corresponding to five-roll regimes in order to keep the relative position of the measurement line with respect to the convection rolls (also see Fig. 1(a)). Figure 10(c) and (d) are examples of time-averaged velocity profiles, $\bar{u}_x(x)$ and $\bar{u}_y(y)$, obtained along the measurement lines Ch4 and Ch1, respectively (see Fig. 1(a)). Fig. 10(b) does not confirm our expectation of a dominating influence of the Hartmann layer according to equation (2) in the parameter range considered here. As expected from Fig. 10(a) a detectable reduction of $u_e/\bar{u}_{y,max}$ can be noticed only for $Q > 4 \times 10^3$ where the Hartmann layer becomes thinner as the Ekman layer. However, in this transition zone the drop of the velocity ratio is not such steep as estimated by equation (2). We assume that Q has to be further increased before the ratio $u_e/\bar{u}_{y,max}$ follows the $Q^{-1/2}$ behavior.

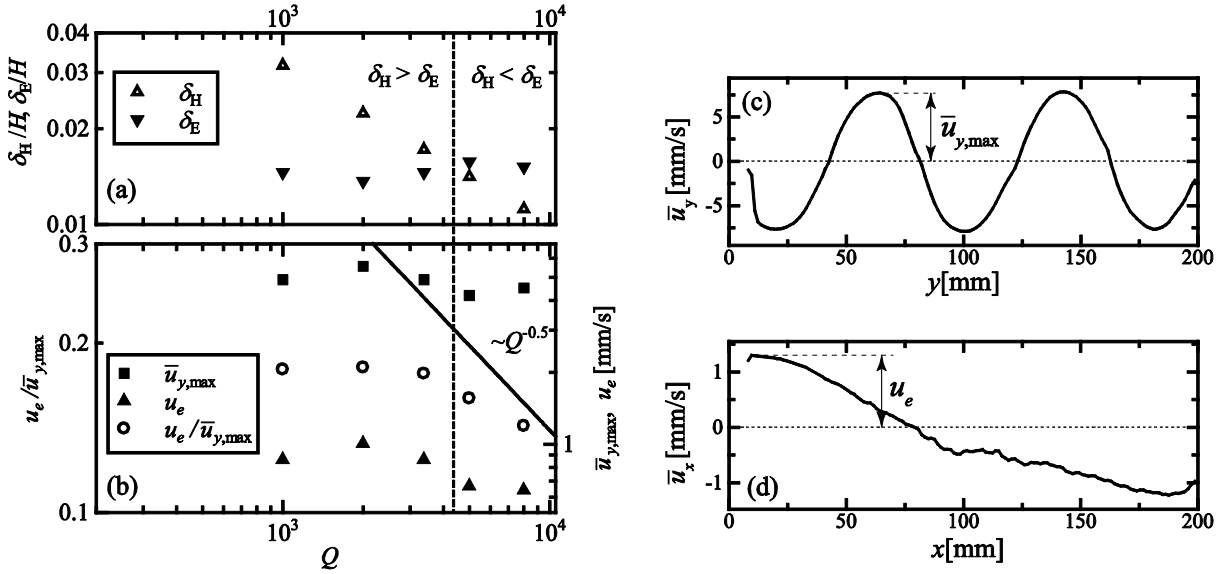

Figure 10: (a) Variation of the thickness of the Ekman layer δ_E and the Hartmann layer δ_H vs. the Q number, (b) Characteristic velocities $u_e, \bar{u}_{y,max}$ and the ratio $u_e/\bar{u}_{y,max}$ vs. the Q number, and time-averaged profiles of (c) the velocity perpendicular to the magnetic field, $\bar{u}_y(y)$ (Ch1) and (d) parallel to the magnetic field, $\bar{u}_x(x)$ (Ch4) for the case Q =2.0 × 10^3 and Ra = 2.1 × 10^4

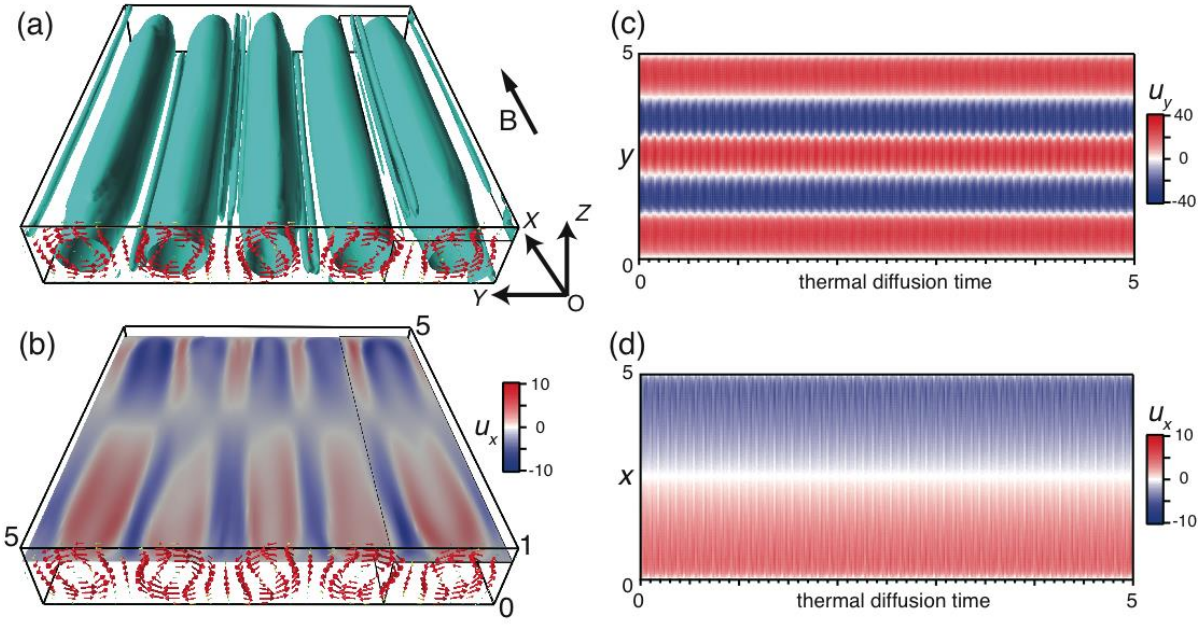

Figure 11: Numerical simulation at Q = 5.7 × 10^3, Ra = 3.0 × 10^4 (Ra/Q = 5.3, 5-roll short OS regime). (a) Iso-surface of Q_{3D}= 0; (b) flow in the direction parallel to the magnetic field (u_x) on the plane $z = 3/4$; (c) velocity perpendicular to B on the y-line at x = 5/2 and z = 3/4; (d) velocity parallel to B on the x-line at y = 5/4 and z = 3/4, the location of the measuring line for (d) is indicated by a thin black frame in (a) and (b); see supplemental material [21] for a movie of (a)

4.2 Occurrence of short period oscillations

Figure 11(a) shows the roll structure obtained by a numerical simulation in a similar parameter range as in the experiment shown in Fig. 4, namely at $Q = 5.7 \times 10^3$, $Ra = 3.0 \times 10^4$, $Ra/Q = 5.3$. Here, the convection rolls and side vortices are uncovered by iso-surfaces of $Q_{3D} = 0$, the second invariant of the velocity gradient tensor. The criterion $Q_{3D} > 0$ indicates vortex-dominated regions [20], and it is widely utilized for identifying 3D flow structures. In this figure, five large counter rotating convection rolls become visible. Another feature that can be recognized in this figure is the existence of additional smaller vortices. These vortices are elongated along the magnetic field lines as well. Singular vortices can be found in the corner region of the cell while small pairs of counter rotating vortices occur in the convergence zone of the neighbouring convection rolls. Their location very close to the top and bottom of the fluid cell above and below the UDV-measuring lines is the reason why these smaller vortices cannot be seen in the velocity distribution shown in Fig. 4(a). The small side vortices play an important role in the stability of the considered flow because such a configuration is supposed to cause flow oscillations and transition to turbulence, as will be shown below. Vortex shedding occurring in the wake of these small elongated vortices can be considered as a reason for a deformation of the initially circular roll cross-section. Such a deformation becomes apparent in form of the short period flow oscillation in the flow measurements. The roll-deformation is visible in figure 11(a). For a better visualization of the roll deformation and how this roll deformation rotates around the roll axis, we refer the reader to the supplementary material (movie) [21].

The Ekman pumping, which is responsible for the flow components parallel to B, is demonstrated in Fig. 11(b) in terms of the spatial distribution of the u_x – velocities at $z = 3/4$. Obviously, this figure obtained by highly-resolved numerical simulations provides a more detailed visualization of the Ekman-induced recirculation compared to the UDV-line measurements. The axial inflow inside the convection rolls occurs over a wide radial range. The return flow towards the walls can be observed in the region between neighbouring convection rolls. The inflow is separated from the return flow by sharp shear layers.

The figures 11(c) and (d) contain the numerical counterpart to the measured spatio-temporal contour plots presented in Fig. 4. The linear velocity profiles were determined for the same positions where the ultrasonic sensors were installed at the experimental setup. Here, the time axis is based on the thermal diffusion time $\tau_\kappa = H^2/\kappa$. The excellent agreement between the numerical findings and the experimental results confirms the reliability of our numerical approach convincingly.

4.3 Transition to 3D structures

In figure 5 of the experimental part of this paper we have shown a measurement obtained at a higher value of $Ra/Q = 33$ where small vortices were detected moving in the u_x – velocity field. The appearance of these vortices can be taken as an indication of the transition from a quasi-two-dimensional to a three-dimensional flow structure in a very early state. In this

section, we want to reveal the characteristic flow structures occurring during this transition. Moreover, our findings demonstrate that the decreasing impact of the Lorentz force (indicated by the growing Ra/Q value) results both in a gradual loss of the two-dimensionality in the flow pattern and a more and more turbulent convection.

Figure 12(a) shows a snapshot of the vortex structure (iso-surfaces at $Q_{3D} = 0$) for a weakly transitional convection at $Ra/Q = 9.3$. This figure illustrates the incipient destabilization of the convection. It can be seen that the small intermediate vortices become unstable and partially interrupted. The perturbation of the small vortices goes along with further deformations of the convection rolls. Now, the recirculating flow induced by Ekman pumping (see Fig. 12(b)) becomes effective by propagating such perturbations along the x - direction parallel to the magnetic field. This becomes obvious in the respective movie [21] and in Fig. 12(d), whereby the Fig. 12(c) and (d) show the temporal evolution of this transitional flow at the corresponding UDV measuring lines. Again, the numerical outcome bears a close resemblance to the experimental results shown in Fig. 5. It is worth to note, that the ratio Ra/Q for Fig. 12 is much smaller than that of Fig. 5, which might be attributed to the difference in the number of rolls (five and four). Migrating local structures appearing near the center of the vessel as displayed in Fig. 5(b) and also in Fig. 12(d) cannot be distinguished in the vortex structure shown in Fig. 12(a). But, the mapping of the axial flow in a horizontal plane at $z = 3/4$ (Fig. 12(b)) shows the formation of local perturbations near the center. In this moment, the Ekman pumping flow is not anymore symmetric with respect to the vessel center line at $x = 5/2$. The perturbations appearing in both the Fig. 5(b) and Fig. 12(d) are obviously generated around the central region of the vessel and move alternatingly to the opposite sides. Our estimations show that the propagation speed of the local structures arising from a deformation of the main rolls and the destabilization of the small aligned vortex pairs corresponds well to the velocity of the Ekman pumping flow. These features are characteristic for transitional flows and produce the complex patterns which were observed in the axial velocity map.

The Chandrasekhar number is reduced in Fig. 13 for studying a further step toward the transition to turbulent convection. Here, a numerical simulation is presented for $Q = 1.76 \times 10^3$, $Ra = 3.0 \times 10^4$ ($Ra/Q = 17$). In figure 13(a) one can see the formation of small vortices just above the convection rolls, whereas its rotational axis is aligned almost perpendicularly with respect to the direction of the convection roll axis. Figure 13(b) shows the u_x – velocity field at $z = 3/4$ and Fig. 13(c), (d) shows the temporal evolution of u_y and u_x, respectively. While the pattern of the primary convection rolls still looks quite stable in time (Fig. 13(c)), the increasing number of sub-vortices becomes apparent in Fig. 13(d). It is hardly possible to determine the origin of these small vortices by means of these contour plots, but a corresponding movie [21] indicates that the vortices detach from the small aligned vortex pairs between the primary rolls. These fragments become stretched and wrapped around the primary rolls. Moreover, they are affected by the roll deformation and the disturbed secondary flow driven by Ekman pumping (see Fig. 13(b)). As a result Fig. 13(d) shows a very complex pattern of the flow velocity parallel to B. The comparison between Fig. 13 and Fig. 12 suggests that the difference in the related flow states is not substantial, however, the

increasing fragmentation of the small aligned vortex pairs and their entrainment into the rotating flow of the convection rolls leads to the rather complex velocity map of u_x shown in Fig. 13(d). Apparently, the deformation of the convection rolls plays an important role in the transition to turbulence. This deformation might be caused by a Kelvin-Helmholtz instability arising from the shear flow between Ekman pumping and its return flow generating alternating small vortices around the center of the vessel, or an oscillatory instability on the main rolls like as known in standard Rayleigh-Bénard convection.

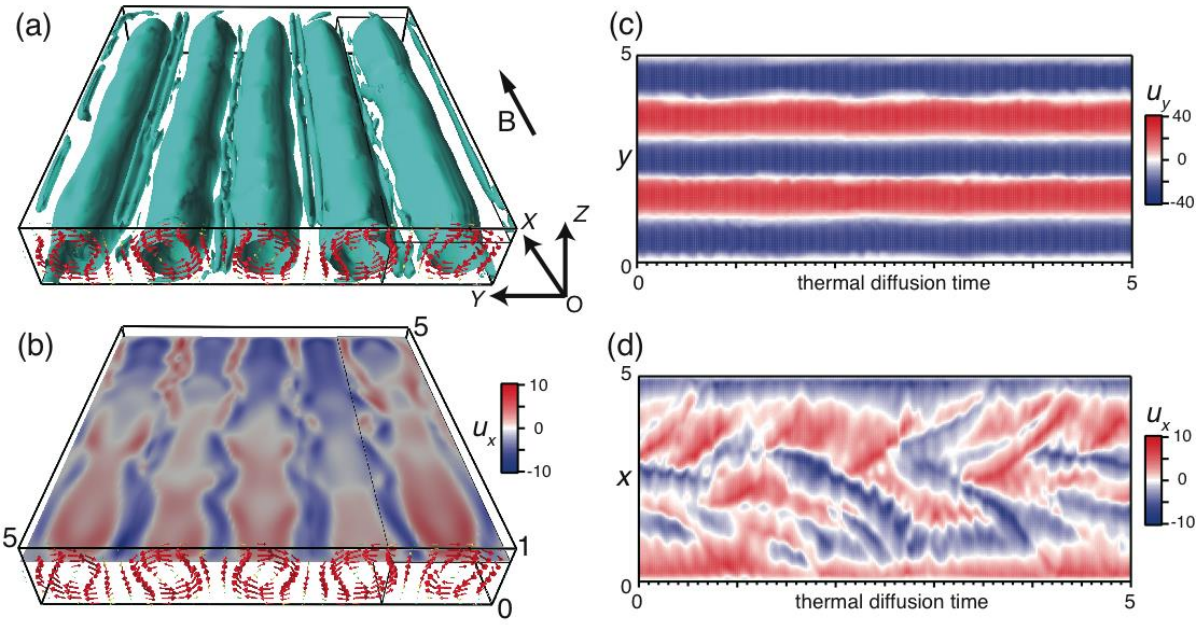

Figure 12: As in Fig. 11, but obtained at $Q = 3.23 \times 10^3$, $Ra = 3.0 \times 10^4$ ($Ra/Q = 9.3$, 5-roll advective regime); see supplemental material [21] for a movie of (a)

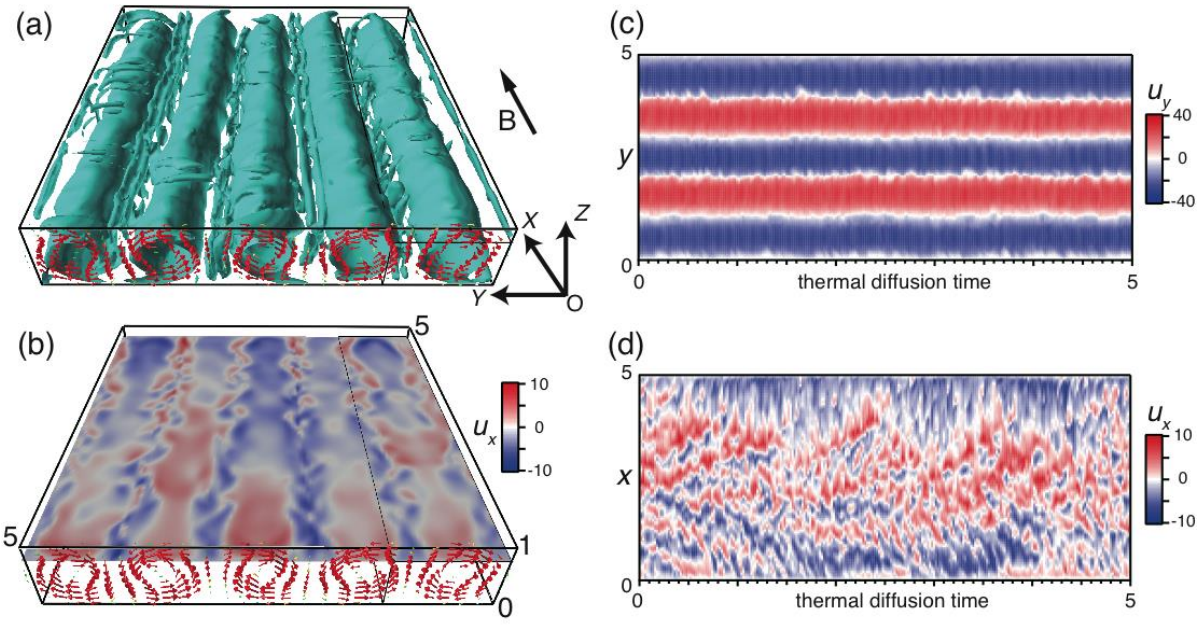

Figure 13: As Fig. 11, but obtained at $Q = 1.76 \times 10^3$, $Ra = 3.0 \times 10^4$ ($Ra/Q = 17.0$, 5-roll advective regime); see supplemental material [21] for a movie of (a)

A further decrease of Q leads to the flow pattern shown in Fig. 14. The size of the side vortices increases and the tendency to a growing disorder in the flow structure becomes more and more pronounced. The side vortices form almost closed vortex tubes winding around the convection rolls. The interaction between these vortices and convection rolls is much stronger than in the previous examples. The corresponding video visualizing the dynamic behaviour of the flow can be found in [21].

Another feature of this transitional state is the occurrence of a standing wave which becomes evident in the spatio-temporal plot of the u_y – velocity in Fig. 14(c), and is also verifiable in the u_x – velocity field of the secondary flow shown in Fig. 14(d). The phenomenon is quite similar to that discovered by flow measurements in Fig. 6. The simulations reveal that the Ekman pumping does not form anymore continuous loops covering the entire fluid vessel, instead the secondary circulation is confined to local patches near the wall.

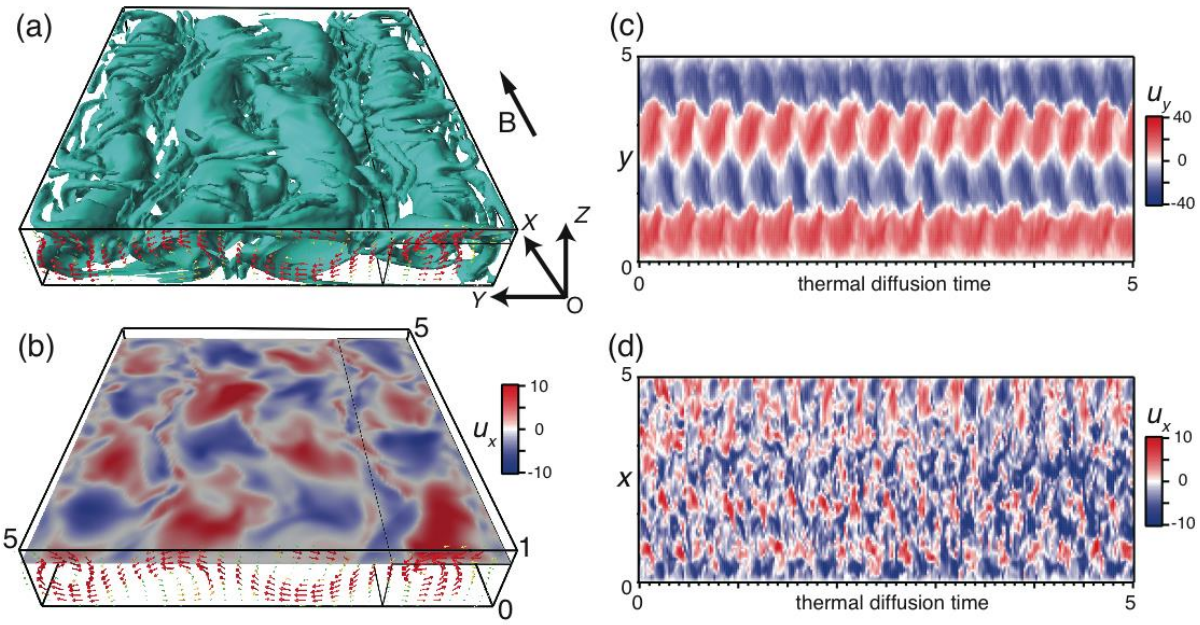

Figure 14: As in Fig. 11, but obtained at $Q = 6.25 \times 10^2$, $Ra = 3.0 \times 10^4$ ($Ra/Q = 64.0$, 4-roll standing wave regime); see supplemental material [21] for a movie of (a)

5. Discussion and Conclusions

The present paper considers the specific case of a Rayleigh-Bénard convection inside an electrically conducting fluid exposed to a horizontal DC-magnetic field. The principal effect of the magnetic field is a reorientation of the convection towards a quasi-2D configuration where counter-rotating convection rolls are aligned with the magnetic field lines. This work

focuses on changes towards an increasingly 3D flow structure occurring as a consequence of a gradually decrease of the magnetic field strength. For the first time we realized successful flow measurements along the direction of the magnetic field. For that purpose, we used special custom-built transducers which are not affected by the strong magnetic field.

The rotating flow in a quasi-2D convection roll between two parallel solid walls is always accompanied by Ekman pumping creating a secondary flow. Inside the Ekman boundary layers the fluid is pumped towards the rotational axis of the convection rolls. The fluid then leaves the boundary layer in the interior of the convection roll and creates a recirculation parallel to the magnetic field lines. Two symmetrical recirculation zones can be found in each convection roll. The magnitude of this circulation is about 1/5 of the rotation speed of the rolls. An increase of Q results in a thinning of the Hartmann layer ($\delta_H \sim Q^{-1/2}$) arising thereby a dominating influence of Joule dissipation. A weakening of the flow becomes visible once the Hartmann layer thickness falls below the thickness of the Ekman layer.

As a key issue, in this paper we addressed the question how the stability of the quasi-two-dimensional flow structure is affected when the Chandrasekhar number is gradually reduced. The declining magnetic field effect enables the development of diverse flow oscillations, which can be attributed to two-dimensional variations of the roll structure and emerging 3D flow effects. In particular, short and long period oscillations occur that can be detected both in the velocity and the temperature field. The frequency of the short period temperature oscillations is identical to the frequency that can be deduced from the velocity field. The analysis of data obtained by measurements of the axial flow component discloses that the flow regime showing short oscillations of the primary roll structure can be subdivided into two regimes. The short period oscillations appear if the shape of the convection rolls deviate from their original circular cross-section. The origin of the short period oscillations can be identified as vortex shedding that proceeds in the wake of the small elongated vortices in the converging zone of the convection rolls. Here, the main flow structure still remains quasi-two-dimensional for sufficiently strong magnetic fields ($Ra/Q < 10$). With increasing Ra/Q ratio ($Ra/Q \geq 30$) distinct deviations from two-dimensionality can be detected at first in the secondary flow driven by Ekman pumping. Small-scale swirling substructures emerge in the flow structure measured along the magnetic field lines. These perturbations are captured by the secondary recirculation and transported towards the Hartmann walls of the fluid vessel. In line with this, the time scales of the long period oscillations are in the order of the Ekman recirculation time. Our numerical simulations show that the long period oscillations are related to roll deformations in axial direction of the convection rolls. This newly discovered regime was called as 4- or 5-roll advective regime. The detailed onset conditions and the mechanism behind the oscillations are rather complex and will be addressed in a future work.

The transition to fully three-dimensional flow further proceeds by increase of Ra/Q to values around 100. Here, we observed a new 3- or 4-roll standing wave regime. This regime appears at a certain Ra/Q - ratio where the previously magnetic field aligned side vortices become unstable, changes their orientation and wind around the convection rolls. Afterwards, these vortices follow the Ekman-induced recirculation and move towards the sidewalls of the vessel. The numerical simulations demonstrated that the secondary flow created by Ekman

pumping cannot form anymore continuous loops covering the entire fluid vessel. Here, the secondary circulation is restricted to local patches near the side walls of the fluid vessel. The spatio-temporal plots of the flow pattern derived from both the experiment and the numerical calculations reveal the features of a standing wave of the convection rolls in this regime.

Another topic, which is reserved for later work, concerns the scaling law for the transition between quasi-2D and 3D flows. Within the scope of this manuscript, the transition was discussed using the parameter Ra/Q. The magnetic interaction $N = Q/Re$ is another important parameter. It is well known from many studies dealing with MHD channel flows or flows in liquid metal layers that the application of a DC magnetic field causes the flow to become two-dimensional when N exceeds a value of 1 (see for instance [13, 15, 22-24]). The present study provides first indications that this scaling could be valid for the RBC, too. In particular, in the experiments the formation of the first three-dimensional structures was observed for $N \approx 0.8$. However, the covered parameter range and the number of the measurements appear to be too small to draw already more definite conclusions regarding the scaling. Therefore, there remains a well-founded answer to this question for subsequent research.

The results in this paper clearly demonstrate that the flow structure of the RBC in a horizontal magnetic field can already become three-dimensional even if the measurements perpendicular to the magnetic field still suggest a stable two-dimensional structure of the primary convection rolls. The deviations from two-dimensionality become apparent first in the secondary flow driven by Ekman pumping. Although the presented effects arising from the secondary flow are often weak compared to the primary convection rolls, their impact on the global flow field and the transition to three-dimensional turbulent flows is essential.

Acknowledgments

Financial support of this research by the German Helmholtz Association within the framework of the Helmholtz-Alliance LIMTECH is gratefully acknowledged. Numerical simulations were performed on the Earth Simulator at JAMSTEC. A part of this work was supported by JSPS KAKENHI Grand No. 24244073.

References

[1] Ahlers, G., Grossmann, S., & Lohse, D. (2009). Heat transfer and large scale dynamics in turbulent Rayleigh-Bénard convection. *Reviews of modern physics*, *81*(2), 503.

[2] Chillà, F., & Schumacher, J. (2012). New perspectives in turbulent Rayleigh-Bénard convection. *The European Physical Journal E*, *35*(7), 1-25.

[3] Burr, U., & Müller, U. (2002). Rayleigh-Bénard convection in liquid metal layers under the influence of a horizontal magnetic field. *Journal of Fluid Mechanics*, 453, 345-369.

[4] Aurnou, J. M., & Olson, P. L. (2001). Experiments on Rayleigh–Bénard convection, magnetoconvection and rotating magnetoconvection in liquid gallium. *Journal of Fluid Mechanics*, *430*, 283-307.

[5] King, E. M., Stellmach, S., Noir, J., Hansen, U., & Aurnou, J. M. (2009). Boundary layer control of rotating convection systems. *Nature*, *457*(7227), 301-304.

[6] King, E. M., & Aurnou, J. M. (2013). Turbulent convection in liquid metal with and without rotation. *Proceedings of the National Academy of Sciences*, *110*(17), 6688-6693.

[7] Zürner, T., Liu, W., Krasnov, D., & Schumacher, J. (2016). Heat and momentum transfer for magnetoconvection in a vertical external magnetic field. *Physical Review E*, *94*(4), 043108.

[8] Chandrasekhar, S. Hydrodynamic and Hydromagnetic Stability, Oxford University Press, Oxford, 1961.

[9] Yanagisawa, T., Hamano, Y., Miyagoshi, T., Yamagishi, Y., Tasaka, Y., & Takeda, Y. (2013). Convection patterns in a liquid metal under an imposed horizontal magnetic field. *Physical Review E*, *88*(6), 063020.

[10] Yanagisawa, T., Yamagishi, Y., Hamano, Y., Tasaka, Y., & Takeda, Y. (2011). Spontaneous flow reversals in Rayleigh-Bénard convection of a liquid metal. *Physical Review E*, *83*(3), 036307.

[11] Yanagisawa, T., Hamano, Y., & Sakuraba, A. (2015). Flow reversals in low-Prandtl-number Rayleigh-Bénard convection controlled by horizontal circulations. *Physical Review E*, *92*(2), 023018.

[12] Tasaka, Y., Igaki, K., Yanagisawa, T., Vogt, T., Zuerner, T., & Eckert, S. (2016). Regular flow reversals in Rayleigh-Bénard convection in a horizontal magnetic field. *Physical Review E*, *93*(4), 043109.

[13] Davidson, P. A. (1995). Magnetic damping of jets and vortices. *Journal of Fluid Mechanics*, *299*, 153-186.

[14] Ekman, V. W. (1905). On the influence of the earth's rotation on ocean-currents. Arkiv för Matematik, Astronomi och Fysik, 2(11), 1-52.

[15] Sommeria, J., & Moreau, R. (1982). Why, how, and when, MHD turbulence becomes two-dimensional. *Journal of Fluid Mechanics*, *118*, 507-518.

[16] Davidson, P. A., & Pothérat, A. (2002). A note on Bödewadt–Hartmann layers. *European Journal of Mechanics-B/Fluids*, *21*(5), 545-559.

[17] Baker, N. T., Pothérat, A., & Davoust, L. (2015). Dimensionality, secondary flows and helicity in low-Rm MHD vortices. *Journal of Fluid Mechanics*, *779*, 325-350.

[18] Plevachuk, Y., Sklyarchuk, V., Eckert, S., Gerbeth, G., & Novakovic, R. (2014). Thermophysical properties of the liquid Ga–In–Sn eutectic alloy. *Journal of Chemical & Engineering Data*, *59*(3), 757-763.

[19] Vogt, T., Grants, I., Räbiger, D., Eckert, S., & Gerbeth, G. (2012). On the formation of Taylor–Görtler vortices in RMF-driven spin-up flows. *Experiments in Fluids*, 52(1), 1-10.

[20] Hunt, J. C. R., Wray, A. A., & Moin, P. (1988). Eddies, streams, and convergence zones in turbulent flows. Center for Turbulence Research Report No. CTR-S88, p. 193.

[21] See supplementary material at …. They are movies for Fig. 11-14(a) and indicating time variations of structure by the iso-surface of $Q_{3D} = 0$. The time duration for these movies is 1 thermal diffusion time.

[22] Sommeria, J. (1988). Electrically driven vortices in a strong magnetic field. *Journal of Fluid Mechanics*, 189, 553-569.

[23] Klein, R., & Potherat, A. (2010). Appearance of three-dimensionality in wall bounded MHD flows. *Physical Review Letters*, 104, 034502.

[24] Eckert, S., Gerbeth,G., Witke, & W., Langenbrunner, H. (2001). MHD turbulence measurements in a sodium channel flow exposed to a transverse magnetic field. *International Journal of Heat and Fluid Flow*, 22, 358-364.